UC San Diego
UC San Diego Previously Published Works

Title

Molecular physiology of contrast enhancement in glioblastomas: An analysis of The Cancer Imaging Archive (TCIA)

Permalink

https://escholarship.org/uc/item/18x108kq

Authors

Treiber, Jeffrey M
Steed, Tyler C
Brandel, Michael G
et al.

Publication Date

2018-09-01

DOI

10.1016/j.jocn.2018.06.018

Peer reviewed

Clinical study

Molecular physiology of contrast enhancement in glioblastomas: An analysis of The Cancer Imaging Archive (TCIA)

Jeffrey M. Treiber [a], Tyler C. Steed [b], Michael G. Brandel [c], Kunal S. Patel [d], Anders M. Dale [e,f], Bob S. Carter [g,1], Clark C. Chen [h,*,1]

[a] Department of Neurosurgery, Baylor College of Medicine, Houston, TX, USA
[b] Department of Neurosurgery, Emory University, Atlanta, GA, USA
[c] Department of Neurosurgery, University of California, San Diego, La Jolla, CA, USA
[d] Department of Neurosurgery, David Geffen School of Medicine, University of California-Los Angeles, Los Angeles, CA, USA
[e] Multimodal Imaging Laboratory, University of California San Diego, La Jolla, CA, USA
[f] Department of Radiology, University of California San Diego, La Jolla, CA, USA
[g] Department of Neurosurgery, Massachusetts General Hospital, Boston, MA, USA
[h] Department of Neurosurgery, University of Minnesota, Minneapolis, MN, USA

ARTICLE INFO

ABSTRACT

The physiologic processes underlying MRI contrast enhancement in glioblastoma patients remain poorly understood. MRIs of 148 glioblastoma subjects from The Cancer Imaging Archive were segmented using Iterative Probabilistic Voxel Labeling (IPVL). Three aspects of contrast enhancement (CE) were parametrized: the mean intensity of all CE voxels (CE_i), the intensity heterogeneity in CE (CE_h), and volumetric ratio of CE to necrosis (CE_r). Associations between these parameters and patterns of gene expression were analyzed using DAVID functional enrichment analysis. Glioma CpG island methylator phenotype (G-CIMP) glioblastomas were poorly enhancing. Otherwise, no differences in CE parameters were found between proneural, neural, mesenchymal, and classical glioblastomas. High CE_i was associated with expression of genes that mediate inflammatory responses. High CE_h was associated with increased expression of genes that regulate remodeling of extracellular matrix (ECM) and endothelial permeability. High CE_r was associated with increased expression of genes that mediate cellular response to stressful metabolic states, including hypoxia and starvation. Our results indicate that CE in glioblastoma is associated with distinct biological processes involved in inflammatory response and tissue hypoxia. Integrative analysis of these CE parameters may yield meaningful information pertaining to the biologic state of glioblastomas and guide future therapeutic paradigms.

© 2018 Published by Elsevier Ltd.

1. Introduction

Glioblastoma is the most common form of primary brain cancer in adults [1]. Despite nearly half of a century of therapeutic development and clinical trials, glioblastoma remains a lethal diagnosis for patients [2]. Molecular profiling of clinical glioblastoma specimens has revealed that tumors with similar histologic appearances harbor distinct molecular physiologies [3–5] and exhibit differing

treatment responses [6]. As such, the "one-size-fits-all" therapeutic paradigm has not yielded a more meaningful improvement in clinical outcome for patients.

The primary approach adopted to study glioblastoma heterogeneity involves surgical acquisition of glioblastoma specimens followed by molecular profiling [7]. While such an approach is effective in an investigative setting, translation of this approach may be costly and may require fundamental changes in the current clinical work flow. Since MRI is the current standard-of-care imaging modality for glioblastoma patients, there is great interest in developing MRI biomarkers that provide molecular information pertaining to the imaged tumor and guidance in terms of subsequent therapeutic intervention [8].

Administration of a gadolinium-based contrast agent is a widely utilized method for assessing patients with intracranial neoplasms [9–13]. While there have been studies to understand the

physiologic processes underlying contrast enhancement (CE), these efforts largely relied on qualitative assessment and involved limited number of patient samples [14–18]. Some established associations with contrast enhancement in GBM include downregulation of proteins maintaining the BBB (e.g., tight junction protein-2) [16], and overexpression of genes associated with the hypoxia–angiogenesis–edema pathway (e.g., Vascular Endothelial Growth Factor [VEGF]) [16,17,19] and extracellular matrix destruction/tumor cell invasion (e.g., matrix metalloproteinase-7 [MMP7]) [20].

Using an automated CE segmentation algorithm and gene expression data available from The Cancer Genome Atlas (TCGA) [21], we analyzed CE through the calculation of distinct CE parameters from 148 glioblastoma subjects in The Cancer Imaging Archive (TCIA). Relationships between these patterns of CE and gene expression profiles of the underlying tumor were explored. We hypothesize that distinct quantifiable features of contrast enhancement represent different cellular processes in glioblastoma. Here, we explore this hypothesis through an analysis of the TCIA and TCGA dataset.

2. Methods

2.1. Imaging preprocessing

A total of 257 subjects from The Cancer Imaging Archive (TCIA; http://cancerimagingarchive.net) were considered for this study. Inclusion criteria included a pre-operative, artifact free contrast-enhanced T1W image and accompanying mRNA expression data from The Cancer Genome Atlas (TCGA). Fourteen subjects were excluded for missing genomic data and sixteen subjects were unable to be processed due to the presence of imaging artifacts (n = 12) or absence of T1W with contrast (n = 4). Fifty subjects with radiographic evidence of skull defects, biopsy tracts, or resection cavities were considered post-operative and were excluded. Subjects with hemorrhage (n = 6), diffuse leptomeningeal enhancement (n = 1), and extra-axial masses (n = 3) were excluded. Nineteen subjects were excluded for having inadequate segmentations due to intrinsic limitations of the algorithm including non-enhancing tumors, tumors with direct contact with dura, and those in continuation with large cerebral blood vessels. The remaining 148 glioblastoma subjects met inclusion criteria and were included in further analyses. Images were processed as described previously [21]. In brief, images were corrected for gradient field non-linearity, bias-fields, and then registered to Montreal Neurological Institute (MNI) 152 nonlinear 1 mm^3 template using Advanced Normalization Tools (ANTs) [22]. For each subject, all available imaging modalities were registered to their native space T1W without contrast. If a T1W image without contrast was unavailable, then a contrast-enhanced T1W image (T1C) was used for intra-subject registration. This "base" image was then registered to the MNI template. The registration transforms were then applied to images in their native spaces to register them to the MNI template. All registrations used an affine transformation, the mutual information similarity metric, and resampled using a linear interpolation. Following registration, Iterative Probabilistic Voxel Labeling (IPVL), a previously described automated segmentation algorithm [21], was used to segment MR images into five tissue components: contrast enhancing tumor, FLAIR hyperintensity, non-tumor contrast enhancement, gray matter, and white matter.

2.2. Contrast enhancement analysis

MATLAB (version 2016a, The MathWorks) and R (version 3.3.1) [23] were used for statistical analyses. In order to adjust for signal variations between scanners and contrast administration protocols, the T1-weighted image with contrast (T1C) were normalized by the median intensity of the segmented blood vessels. The mean intensity of all normalized voxels within contrast enhancing tumor segmentation was quantified as CE_i (Fig. 1A). We quantified heterogeneity (CE_h) by calculating the Shannon entropy [24], an intensity-independent measure of data variation, of the entire CE segmentation registered to native space (Fig. 1B). Finally, we determined the fraction of contrast enhancing tumor to volume of necrosis by performing a volumetric filling of the contrast enhancing portion. The volumetric ratio of CE tumor to filled CE segmentation was calculated as CE_r (Fig. 1C). The 'moments' package in R was used to assess the skewness and kurtosis of each parameter which was compared to a normal distribution using the D'Agostino and Anscombe-Glynn tests, respectively.

2.3. Genomic data

Level 3 probe collapsed, median normalized messenger RNA (mRNA) expression data (Affymetrix HG U133A array) was downloaded using the TCGA Data portal in June 2014. We identified genes that were differentially expressed by at least 1.2 fold-change between tumors with higher or lower than median CE parameter and performed Benjamini-Hochberg correction [25]. After correction, genes with $p < 0.05$ were considered significant. The list of differentially expressed genes were functionally annotated using the Database for Annotation, Visualization, and Integrated Discovery [26,27] (DAVID; https://david.ncifcrf.gov/) to determine cellular processes mediated by the differentially expressed genes. Genomic subtypes (Proneural, Neural, Classical,
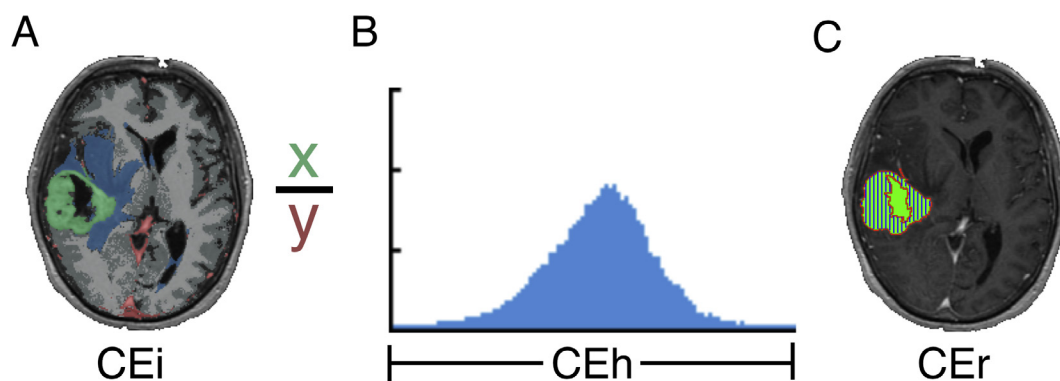
Fig. 1. (A) CE_i is calculated as the mean intensity of all voxels within the contrast enhancing tumor (green) divided by the median intensity of voxels within the blood vessel segmentation (red). (B) CE_h is calculated as the entropy of the intensities within the contrast enhancing segmentation. (C) CE_r is calculated as the number of voxels within the contrast enhancing segmentation (area outlined in red with blue stripes) divided by the number of voxels within the filled contrast enhancing segmentation (green).

Mesenchymal) were determined using single sample gene set enrichment analysis [5,28]. Original source data used in this study had been anonymized according to standard HIPAA protocol and all contributing sites had approval by their institutional review board.

3. Results

3.1. CE parameterization

We derived three CE metrics described in Methods and shown in Fig. 1. The mean normalized intensity of CE of the tumor was calculated as CE_i. The total variation in CE intensity, or CE heterogeneity, was calculated as CE_h. The ratio of CE voxel to total tumor volume was determined as CE_r. Examples of CE segmentation are shown in Fig. 2.

Overall, we found that the tumors with known glioma CpG island methylator phenotype (G–CIMP) were minimally enhancing and exhibited poorly defined tumor boundaries and therefore unable to reliably extract CE_i, CE_h and CE_r from these G–CIMP glioblastomas ($n = 4$). In this context, the 4 G–CIMP subjects were excluded from further analysis. The clinical data and imaging parameters of the remaining TCIA cohort are shown on Table 1. There were no significant differences between the proneural, neural, classical, and mesenchymal subtypes of glioblastomas as a function of the three CE metrics. The median cut-offs, kurtosis, and skewness of these parameters are displayed in Table 2.

3.2. Gene expression analysis

To better understand the biologic processes contributing to differences in contrast enhancement, we identified genes that were
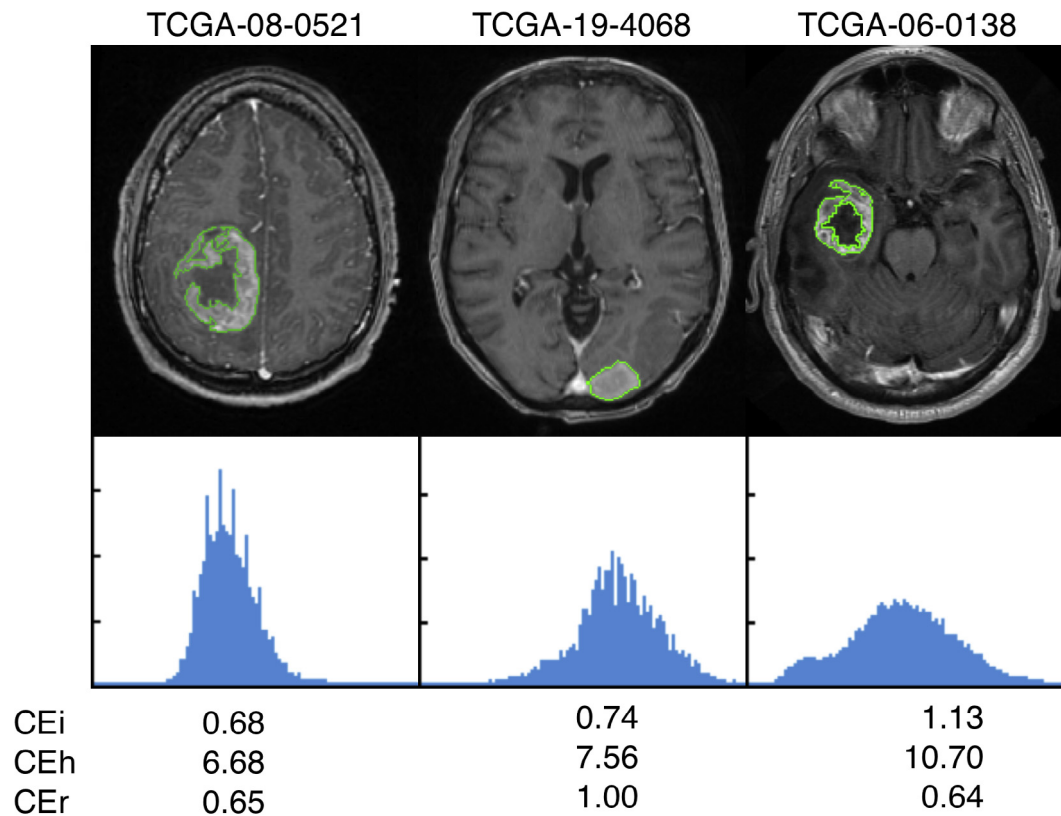
Fig. 2. Example subjects demonstrating their CE segmentations (green outline) and imaging parameters (bottom). Visualization of the CE intensity heterogeneity is shown as intensity histograms (blue).

Table 1
Subject clinical and imaging data stratified by glioblastoma molecular subtype.

Variable	All	Proneural	Neural	Classical	Mesenchymal
n	144	33	29	40	42
Age, y, mean ± SD	61.2 ± 13.5	59.8 ± 14.3	62.2 ± 12.6	60.8 ± 15.6	62.1 ± 11.4
KPS, mean ± SD	77.48 ± 14.63	75.86 ± 11.19	77.14 ± 20.28	74.71 ± 14.19	81.71 ± 13.17
OS, d, mean ± SD	393.6 ± 326.6	295.2 ± 348.9	403.5 ± 292.8	459.3 ± 299.7	401.0 ± 347.8
PFS, d, mean ± SD	266.1 ± 268.0	249.7 ± 353.7	239.9 ± 172.5	258.4 ± 176.1	303.3 ± 312.7
CE_v, mm^3, mean ± SD	31949 ± 21546	30684 ± 19891	34953 ± 23907	32985 ± 20907	298823 ± 22162
CE_i, mean ± SD	0.82 ± 0.13	0.81 ± 0.15	0.85 ± 0.14	0.78 ± 0.11	0.84 ± 0.13
CE_r, mean ± SD	0.75 ± 0.14	0.76 ± 0.14	0.75 ± 0.12	0.74 ± 0.14	0.76 ± 0.14
CE_h, mean ± SD	8.33 ± 1.65	8.16 ± 1.43	8.61 ± 1.72	8.07 ± 1.26	8.51 ± 2.04

KPS: Karnofsky Performance Status. OS: Overall Survival. PFS: Progression Free Survival. CE_v: Contrast Enhancing Volume. CE_i: Contrast Enhancing Intensity. CE_r: Contrast Enhancing Ratio. CE_h: Contrast Enhancing Heterogeneity.

Table 2
Median Cut-offs, Kurtosis, and Skewness of the CE Parameters.

Variable	Median ± MAD	Kurtosis	p	Skewness	p
CE_v, mm^3	29287.5 ± 21498.44	3.79	0.068	0.93	<0.001
CE_i	0.81 ± 0.15	2.56	0.257	0.33	0.098
CE_r	0.77 ± 0.14	2.38	0.051	-0.33	0.097
CE_h	8.31 ± 1.48	7.66	<0.001	1.37	<0.001

KPS: Karnofsky Performance Status. MAD: Median Absolute Deviation. Contrast Enhancing Volume. CE_i: Contrast Enhancing Intensity. CE_r: Contrast Enhancing Ratio. CE_h: Contrast Enhancing Heterogeneity.

Table 3
DAVID functional enrichment analyses. The four largest clusters with an enrichment score > 2.5 for each imaging parameters are shown. Gene lists are from the largest pathway for each cluster.

Cluster	Enrichment Score	p	Genes
CE_i: Increased			
Signal peptide/disulfide bond/glycoprotein	12.3	<0.01	ADORA3, SCN3B, MMP9, GABRB1, TLR1, TLR2, CD53, TLR5, MOG, TLR7, IL10, SLC7A7, SLC2A5, LILRA2, CSF3R, VNN2, EBI3, INA, F12, PHYHIP, C5AR1, CLCA4, OLFML2B, PTPRN, C1QA, LILRB1, C1QB, CD37, NPC2, F5, CCR5, CD33, ST14, RELN, CHGB, IBSP, C3AR1, IL1R2, SCN1B, ENPP2, ITGAE, APOC2, IFI30, ITGB2, CALR, ITGAM, SLC11A1, P2RY6, SLC29A3, REG1B, EPHB6, REG1A, FOLR2, ITGAX, ENTPD3, SRGN, CSF1R, ADAM28, HCN2, MGAT4A, ST6GAL1, GABRA2, GABRA1, GABRA4, CHI3L2, SLAMF8, SERPINI1, CACNA2D3, SLCO2B1, KCNK1, GPR37, CD300A, CLEC7A, IER3, MSR1, LY86, UCHL1, IL21R, HP, GPR88, CDC42, ASGR2, TNFRSF11A, EVI2A, HPSE, AOAH, CREG1, EVI2B, SV2B, FCGR3B, DPEP2, PILRA, LAIR1, LY96, SAA4, PCDH8, SIGIRR, CD163, GRM3, CHGA, ADRB2, CD86, FOLH1, SIGLEC7, CNTN2, CTSC, TREM2, CTSH, PTAFR, TF, PRF1, CPM, C3, CCR1, FPR1, GPR65, SIGLEC9, PCSK1, NPTX1, SLCO1A2, ACSL1, SYN1, IL10RA, RNASET2, FCGR1A, LY6H, CD4, C2, GPNMB, NEFL, NEFM, B4GALNT1, KLK6, PTPRC, MAG, RNASE2, SLC8A2, LIPA, RNASE3, SELL, RNASE6, SLC12A5, OR7A5, CPVL, SNAI1, CD180, CD1D, P2RY13, SLC17A6, STAB1, CDH19, FCGR2A, CD14
Immune response	11.2	<0.01	LST1, S100A8, C3, LY86, TLR1, S100A9, TLR2, IFI30, HP, TLR5, TLR7, BTK, NOD2, LILRA2, FCGR1A, MAP3K8, PYCARD, CD4, C2, CFD, CSF1R, SYK, LAIR1, CARD9, LYN, LY96, HCK, LGALS9, CD180, S100A12, CD1D, LILRB1, C1QA, C1QB, CD86, LAT2, IRF5, CD300A, LILRB4, LRMP, FCGR2A, CLEC7A, VSIG4, CD14
Transmembrane domain	8.4	<0.01	ADORA3, S100A8, AQP9, SCN3B, AIF1, SNCA, S100A9, CD53, MOG, BTK, LILRA2, VNN2, HIGD1B, SYK, SH3GL3, C5AR1, CLCA4, NCF1, NAV3, PTPRN, DCTN2, LILRB1, LHFPL2, CD37, CCR5, LILRB3, CD33, ST14, LILRB4, CX3CR1, RYR2, VSIG4, BIN2, TM6SF1, IL1R2, CDK5R2, SCN1B, GNAI1, ENPP2, MMD, PEX5L, ATP6V0B, CAMKV, SLC11A1, EPHB6, SLC29A3, FCER1G, SLC31A2, BLNK, TYROBP, MGAT4A, ST6GAL1, FBXO2, NCKAP1L, SLAMF8, KCNK1, SYNGR3, S100A12, RGS2, CD300A, MAP7, CLEC7A, MSR1, AP1B1, SPI1, LTC4S, GJA4, GPR88, RTN2, ASGR2, NOD2, TNFRSF11A, ATP5O, FCGR3B, DPEP2, LYN, CACNG3, CD163, SIGIRR, EPB41L3, GRM3, DOK3, LRMP, PRF1, RAB3A, CCR1, GPR65, FPR1, CLDN11, APBB1IP, AMPH, PGBD5, ACSL1, FCGR1A, ALOX5AP, IL10RA, LY6H, TBXAS1, SLC8A2, COX7A1, SELL, HCLS1, ATP1A3, CD180, CD1D, LSP1, P2RY13, PDE2A, STAB1, CDH19, CHN2, FCGR2A, TMEM176B, CD14, TMEM176A, GABRB1, TLR1, TLR2, TLR5, TLR7, SLC7A7, FAM49B, DYSF, CISD1, SLC2A5, CSF3R, STMN2, FA2H, BASP1, IGSF6, LAT2, VAMP8, C3AR1, LST1, ITGAE, NINJ2, HMP19, ITGB2, FXYD7, ITGAM, FTH1, P2RY6, KCNS1, PPP1R16B, DOCK2, LAPTM5, ITGAX, FOLR2, ENTPD3, CSF1R, CYP19A1, ADAM28, HCN2, TESC, GABRA2, GABRA1, GABRA4, CPNE6, CACNA2D3, SLCO2B1, CORO1A, GPR37, UCP2, TRAF3IP3, SYT13, IER3, IL21R, UCHL1, ARHGAP15, SYNGR2, MBP, CDC42, HPSE, EVI2A, HMOX1, SV2B, EVI2B, DLG2, RHOG, ATP8B4, PILRA, RHOH, LAIR1, MPP1, TMEM70, STXBP2, DHRS9, PCDH8, DDN, TRPM2, STOM, ADRB2, DHRS3, CHGA, CD86, FOLH1, SIGLEC7, CNTN2, TREM2, PTAFR, CPM, CABP1, SIGLEC9, NDUFB1, NDUFB2, SLCO1A2, CD4, GPNMB, MS4A6A, B4GALNT1, TCIRG1, MS4A4A, PTPRC, MAG, PLP1, HCK, SLC12A5, OR7A5, RGS19, MAL, RCAN2, SLC17A7, CYBA, SLC17A6, MGST2
SH3 domain	8.0	<0.01	SH3GL3, FYB, OSTF1, MPP1, NCF2, LYN, NCF1, GRB2, HCLS1, HCK, MYO1F, SAMSN1, VAV1, BTK, SLA, AMPH, ARHGAP4, DOCK2, PLCG2, BIN1, SH3TC1, DLG2
CE_i: Decreased			
DNA damage repair	26.6	<0.01	XRCC5, MMS19, NBN, XRCC2, SETX, NONO, MUTYH, RAD21, DDX11, FANCI, USP10, TLK1, TLK2, PMS1, FANCC, BRCC3, REV1, DTL, LIG1, USP1, POLE, FMR1, CDK9, TOPORS, CDK7, HERC2, RBBP6, CDK2, RAD50, RAD51, RAD1, EYA4, DCLRE1A, CCND1, RFWD3, HUWE1, RIF1, BAZ1B, TIMELESS, UBR5, RUVBL1, PSME4, GADD45A, CLOCK, PPP5C, USP7, HMGB1, FOXM1, UNG, TIPIN, PRKDC, CHEK1, BCCIP, RPA1, ERCC5, MDC1, PALB2, ERCC3, ERCC4, FEN1, ERCC2, SSRP1, MSH6, MSH2, NFRKB, SMC5, SMG1, BRCA2, SMC6, ATAD5, CEP63, RAD54L, SMC3, ATM, UIMC1, ATRX, PAXIP1, CUL4A, VCP, SFPQ, PCNA, SUPT16H, CUL4B, SMC1A, ABL1, CHAF1A, CHAF1B, BARD1
ATP binding	23.1	<0.01	XRCC5, KIFC1, TARS2, ADCY6, CLK1, MAP3K7, DDX18, DDX11, DHX38, CLK4, DYNC2H1, RAB23, PIK3CA, TLK1, TLK2, DHX35, DHX30, GTPBP4, OPA1, ROCK1, ROCK2, PIK3CB, LIG1, AARS, UBE2J1, EIF2S3, MARK3, RFC5, MAPK6, RFC1, BAZ1B, EIF2AK2, KIF4A, GNAI3, NEK1, OAS3, CHEK1, EPHB3, QRSL1, SUPV3L1, NAT10, DHX57, DHX8, DHX9, KIF3B, MKI67, ACACA, DDX1, TRIO, YTHDC2, OXSR1, DDX5, RAD54L, SEPT11, ATM, GART, NOLC1, RAD54L2, ABCF1, SPG7, SEPHS1, UBE2G2, TTLL4, GNL3L, HELZ, MTHFD1, TOP2B, TOP2A, NT5E, NT5C, CDC6, ABCE1, CCT6A, GMPS, RAD50, RAD51, GNAQ, RIPK1, RRM1, RAB5A, RUVBL1, SLC27A3, ALDH18A1, BMS1, SNRK, DDX19A, BUB1, DHX15, DHX16, UPF1, NPR1, NPR2, ACLY, SPATA5L1, ATRX, PAPOLA, TEX14, CSNK1E, PAICS, PRPF4B, STK38, GNA11, HBS1L, IDE, EIF5B, CASK, RPS6KB1, SETX, CSNK2A2, DDX27, CSNK2A1, DDX23, DDX21, GNL2, GNL1, GNL3, WEE1, SMARCA5, DDX31, SMARCA2, EP400, SEPT9, SMARCA4, FGFR1, FGFR3, BLM, BMPR2, CTPS2, ABCA3, RRAGB, KARS, PTK2, DDX3X, RHOBTB2, DDX42, ERCC6L, TAF1, RYK, ATAD2, SMG1, ATAD5, PLK4, MYO10, VCP, GTF2F2, HSPD1, SMC1A, ABL1, MYH10, KIF23, KIF22, SKIV2L2, CAD, PIP5K1A, FER, MCM7, KIF14, KIF11, KIF15, PRKCI, PKN2, CDK9, MCM2, CDK7, MCM3, MCM4, MCM5, CDK2, MCM6, TARS, PRKD2, ACVR2B, BUB1B, PRKD3, BTAF1, PRKDC, IARS, CHD9, IGF1R, CHD7, MAP3K2, MAP3K1, TOR1B, LARS, CHD1, GPSM2, GUF1, YES1, ERCC3, EHD1, PIK3R4, CHD4, ERCC2, HSPA9, MSH6, MSH2, SMC5, SMC6, RAF1, CENPE, SMC3, SMC4, THRAP3, BMPR1A
Transcription regulation	22.3	<0.01	XRCC5, SLC2A4RG, STAT5B, HIRA, MED24, MED8, RORB, RORA, ZNF254, NONO, MAP3K7, PRIM1, BRPF1, DDX11, PATZ1, ZNF43, IKBKAP, ZNF45, MED12, MECP2, HMG20A, ZHX3, MED14, HMG20B, MED13, ZNF37A, ZNF500, RFC1, ASCC2, BAZ1B, MED17, TGIF1, TGIF2, VGLL4, EIF2AK2, MYBBP1A, CRTC3, ZNF611, ZNF131, TAF9B, ZNF510,

Table 3 (continued)

Cluster	Enrichment Score	p	Genes
			ZNF232, ZNF230, MYBL1, HESX1, ZNF227, HTATSF1, ARNTL2, VEZF1, PLAGL2, HIP1, ZBTB48, KLF7, MAML1, ASXL1, DDX1, ZBTB40, TFCP2, DDX5, SFMBT1, ZBTB43, ZNF629, NOTCH2, NOTCH1, PAXIP1, SAP130, RNF4, PPRC1, SUPT16H, ZNF117, CHAF1B, ZNF219, TAF1B, TAF1C, ELF2, BACH2, ZNF532, CCNT1, ZEB1, ZNF10, DAXX, DNAJC17, RRN3, ZNF148, ANP32A, BRD7, USP16, BRD9, ATF7IP, CTBP1, AR, RBBP5, RBBP4, POLR1E, SNAPC4, GMEB2, ZNF337, TTF1, POLR1B, SPEN, ZBTB24, MXD3, ZNF334, NOC2L, MED6, BRWD1, CCND1, CHMP1A, TAF12, ZNF136, NAB2, ASH1L, NAB1, USP21, RUVBL1, RBM39, ZNF551, NSD1, CLOCK, MED1, ZNF273, ZBTB6, ZNF654, ZNF175, POLR2B, NPAT, PER2, PER1, WAC, LIMD1, PER3, BAZ2B, ETV4, ZNF263, SSRP1, TBX3, PHF10, ILF3, TRIM24, POLR3E, ZNF665, POLR3D, ATRX, MNAT1, UBTF, JMJD6, SFPQ, ZNF764, MPHOSPH8, MMS19, RBM15B, ZNF451, ZXDC, CNOT1, FOXO3, CNOT7, PNN, CSNK2A2, ESF1, CSNK2A1, SMARCD2, CASP8AP2, TARDBP, PSIP1, DDX21, TGS1, ZNF446, GABPB2, SS18L1, ZNF592, RBL2, ZNF8, ARID1A, SLTM, SUZ12, TRIM33, TIMELESS, MGA, SMARCA2, SMARCA4, FGFR1, HMGB2, ZNF430, CNBP, SETD1A, SOX5, TRRAP, MEIS1, CXXC1, DDX3X, ZNF426, SLC30A9, TFDP1, SETDB1, TAF1, ZMYM2, TAF6, TAF5, ATAD2, TEAD1, WHSC1, MED13L, UIMC1, SAFB2, SREBF2, PHF2, SMARCC1, GTF2F2, DNMT1, ZNF318, ZNF83, E2F3, RSF1, YLPM1, ZNF202, CTCF, ZKSCAN1, ZKSCAN5, FUBP1, BZW1, PCGF2, GTF2A1, RTF1, NFX1, KHDRBS1, SOX13, FOXJ2, SOX12, ZFX, PKN2, CDK9, CDK7, FOXJ3, CCNL2, EYA4, BPTF, NCOA3, NCOA6, ZNF711, JMJD1C, BCLAF1, FOXM1, CTNND1, TRIB3, WBSCR22, NR3C1, TCF7L2, CHD9, CHD7, RGS12, CDYL, SAFB, CEBPZ, NFAT5, CHD1, ERCC3, NFATC3, GTF3C4, CHD4, ERCC2, GTF3C3, BAHD1, NFRKB, CREB5, CREB, SIRT7, ADNP2, RPAP1, SP3, THRAP3, SETD2, TBL1X, NFIB
Mitosis	18.2	<0.01	KIFC1, PRC1, KNTC1, RPS6KB1, CSNK2A2, CSNK2A1, RAD21, CASP8AP2, TLK1, TLK2, CCNA2, ASPM, CDCA3, STAG1, ANAPC1, RBL2, LIG1, HMG20B, TACC3, NCAPD3, WEE1, NCAPD2, DCLRE1A, MAPK6, TIMELESS, SPAG5, BIN3, SEPT9, GNAI3, NEK1, TIPIN, CHEK1, NIPBL, NCAPG2, FBXO5, CLASP1, NUDC, TFDP1, ERCC6L, PRPF40A, CKAP2, TAF1, MKI67, BRCA2, GAS1, CDC27, SEPT11, ATM, CHAF1A, SMC1A, CHAF1B, KIF23, NBN, E2F3, CCNT1, NDE1, MCM7, FANCI, BRD7, TPR, USP16, GOLGA2, ZW10, KHDRBS1, SPECC1L, CDC6, KIF11, RBBP4, BRCC3, POGZ, DSN1, TPX2, PKN2, NUSAP1, MCM2, CDK7, MCM3, MCM4, ECT2, MCM5, RAD50, CDK2, MCM6, CHMP1A, CCND1, RAB11FIP3, RIF1, BUB1B, SIAH1, SIAH2, MAPRE1, RUVBL1, GADD45A, PARD3, FOXM1, BCCIP, NR3C1, CEP55, MDC1, NCAPG, USP39, NPAT, BUB1, PAFAH1B1, ZWILCH, FBXW11, PDS5A, NASP, SMC5, CENPF, CENPE, CEP63, SMC3, SMC4, CDC25B, MNAT1, SON, TEX14, CUL4B
CE_r: Increased			
Transcription regulation/ zinc finger region	5.4	<0.01	XRCC2, PPP2R5A, NELL1, ASCC1, RORB, MED23, RORA, CLK1, XRCC1, MXI1, PRKX, CLK2, CLK4, ZNF248, YEATS2, STAG3, PTBP2, OGT, DHX32, STAG2, ZNF43, RCOR3, PIK3CB, LIG1, EMX2, UBR4, UBR2, DCLRE1C, ZNF236, RPS19, MAPK6, CEP350, MTF2, UBR5, PDE4DIP, PIAS2, NUP43, ZIM2, TRAPPC2, ZNF611, ZNF133, PIN4, COIL, PLAGL1, HEXIM1, ZNF223, SUPT7L, SLC4A1AP, NKRF, IKZF5, MAP2K1, SMAD7, CLCC1, YTHDC1, ACACB, HNRNPA1, ATM, SHOX2, DMTF1, RWDD3, ATAD2B, ZNF536, ZNF292, ELF2, BACH2, EZH1, SENP5, ZNF345, ZNF14, OFD1, ZNF350, PBXIP1, HSF2, NARF, USP15, ZNF493, ZCCHC11, SNAPC4, ZFP30, EXOSC5, ZNF142, ZNF337, ADNP, MBD5, PRPF39, TLE4, ZNF143, HERC2, TTF2, ZNF334, ZNF692, ZNF136, PFDN4, MGEA5, FOXC1, RBM39, NHEJ1, NOL12, REV3L, YPEL1, USP3, SCAPER, ZBTB11, SCML1, ABI1, ZNF652, SF3B1, NR1D1, MORC3, NR1D2, RB1CC1, NPAT, SPATA2, BAZ2B, ZNF562, ZNF266, CCNB1IP1, ZNF264, PDS5B, JARID2, ZNF667, RPS6KA5, RLF, DUSP2, ANKRD49, BCORL1, BNIP3L, ZBTB5, APBB3, TJP2, RBM15, ZNF571, MPHOSPH8, TOB1, MORF4L1, XPO1, SEPT4, ZNF451, RBM5, KNTC1, CBX7, SMNDC1, CASP8AP2, TIA1, EED, ZNF180, CUTC, PMS1, SS18L1, SNRPA1, MYO6, RBL2, FMR1, ZNF7, NPEPPS, CSTF2T, DCUN1D1, TRIM33, MGA, TESK2, AKAP7, ZNF432, ZNF587, MYNN, FBXO11, ZNF586, CAMTA1, ZNF331, NR2C1, DAZAP1, CEPT1, FBXW7, DDX46, TCERG1, TTBK2, TFDP2, SSX2IP, ZMYM2, ZMYM1, TAF5, LPP, ZMYM3, ARID3B, LHPP, HDAC5, CRBN, CDKN1B, CDKN2AIP, PNRC1, HIVEP1, SCMH1, PLEKHA1, ZNF83, EPS15L1, PDCD4, ZKSCAN4, TMF1, SETMAR, S100PBP, HIST3H2A, MDN1, ZCCHC8, EGR3, REV1, KHDRBS2, PKN2, CCNL1, LDB2, LAS1L, LPIN1, CCNL2, RIF1, TNNI3K, JMJD1C, MDM1, PEG3, BTAF1, PPM1A, EGLN3, CDC73, CALCOCO1, TSPYL1, TSPYL2, PLEKHO1, GTF3C5, ZNF701, SIRT5, SIRT7, PPP1R13L, SIRT1, FBL, RSBN1, RPAP2, DBP, HIF3A, UCKL1, PPP1R13B, DENND4A
ATP binding	3.8	<0.01	SEPT4, DYNC1LI1, TRPV1, TTLL4, PIP5K1B, TTLL7, CLK1, PRKX, ATP2B2, PEX1, CLK2, CLK4, NT5C2, VPS4B, ATP8B1, RAPGEF4, MDN1, DHX32, GTPBP2, GTPBP3, MYO6, PIK3CB, LIG1, PI4KA, PKN2, PFKP, ABCC10, TTF2, CLPX, MAST3, PRKCQ, PANK2, MAPK6, ATP9B, EIF4A2, ROR1, TNNI3K, TESK2, AKAP7, MAP3K14, MAP3K12, ABCA8, FGFR2, RAB3A, BTAF1, GCLC, DNAH17, WARS2, RRAGB, RAB40B, ABCA5, IGF1R, KRAS, DDX46, TTBK2, CKMT2, ENTPD3, STK38L, ACSL6, DHX58, MYO5C, TRMU, MAP2K1, MAT2A, ACACB, ATM, RAB33B, NTRK3, NUBPL, RPS6KA5, PYGM, ULK1, UCKL1, AACS, ABCC5, CLCN4, ATAD2B, TRIT1, ATP7B, BMPR1A
UBR-type zinc finger region	3	<0.01	UBR5, UBR4, UBR2, FBXO11
Protein ubiquitination	2.7	<0.01	USP6, HECW1, UBE3B, USP3, USP9X, ZNF451, MYLIP, ASB13, SENP5, KLHL3, RAB40B, CUL2, TRIM2, FBXW7, KRAS, KLHL22, PELI2, FBXO9, USP15, USP33, FBXO46, CCNB1IP1, PELI1, UBR4, HERC5, UBR2, HERC2, HERC1, MARCH5, WSB1, DCUN1D1, CRBN, TRIM33, UBR5, TRPC4AP, USP20, PIAS2, FBXO11
CE_h: Increased			
Extracellular Matrix	3.1	<0.01	ASPN, COL4A1, SPOCK2, SPARCL1, LUM, COL3A1, EFEMP1, MMP19, DCN, COL5A3, COL5A1, COL4A5, ADAMTS9, COL6A3, ADAMTS1, COL1A1, SPON2, LOXL2, FN1, ANGPTL4
Platelet granules	2.7	<0.01	APP, VEGFA, ADAMTS1, THBS1, COL5A1, FN1, PCOLCE2, CYR61
CE_h: Decreased			
Mitosis	4.0	<0.01	KIFC1, PPP1CA, CCND1, LIG3, CHEK2, ZWILCH, TACC3, CDCA3, NCAPD2

differentially expressed between high and low parameters (CE_i, CE_h, and CE_r) based on a median cutoff. The differentially expressed genes were annotated using the DAVID functional annotation bioinformatics microarray analysis (https://david.ncifcrf.gov). The results of this analysis are summarized in Table 3. We found that high CE_i was associated with increased expression of genes required for the inflammatory responses including signal peptides ($p < 0.01$) and transmembrane proteins required for immune response ($p < 0.01$) and decreased expression of genes required for DNA repair ($p < 0.01$). Of note, inflammatory processes have been shown to suppress the expression of DNA repair genes [29].

High CE_h was associated with increased expression of genes that regulate remodeling of extracellular matrix ($p < 0.01$) and genes encoding proteins found in the platelet granules ($p < 0.01$). The platelet granule proteins (including VEGFA) play key roles in regulating the permeability of endothelial cells [30,31]. In general,

increased transcription of these ECM remodeling genes and endothelial permeability regulating genes are observed during the process of tumor migration or invasion [32,33]. High CE_h was also associated with decreased expression of genes required for mitosis (p < 0.01), a process that is suppressed during tumor migration or invasion [34].

High CE_r was associated with increased expression of genes encoding zinc-finger transcription factors (p < 0.01), ATP binding proteins (p < 0.01), and protein required for ubiquitination and proteasome function (p < 0.01) [35]. These genes are typically up-regulated in response to stressful metabolic states, such as hypoxia and starvation [36–38]. This finding likely reflects the cellular response to the microenvironment adjacent to the non-enhancing necrotic core of glioblastoma [39].

4. Discussion

Historically, CE in glioblastoma patients is thought to reflect tumor induced altered vascular permeability [40]. This interpretation is largely supported by previous studies that correlated qualitative assessment of MR findings and gene expression patterns [14,16,17]. Diehn et al. (2008) studied MRI and molecular profiles of tumor specimens from 22 glioblastoma patients and report association between the presence of CE and the expression of VEGF, a key modulator of angiogenesis and cellular response to hypoxia [17]. Pope et al. (2008) recapitulated this finding in a study of 52 glioblastoma patients [16]. Similarly, Jamshidi et al. (2014) studied the MRI and molecular profiles of 23 patients and showed an association between tumors rated as being highly contrast enhancing and VEGF related angiogenic factors [14].

The association between dysregulated vascular permeability secondary to altered VEGF expression and CE was confirmed in our study of 148 glioblastoma subjects. Additionally, our study presented four new findings. First, the intensity of CE may serve as an imaging proxy for inflammation mediated altered endothelial permeability [41,42]. Second, the heterogeneity in CE likely represents the spectrum of altered vascular permeability associated with distinct steps in the process of glioblastoma migration and invasion [32,33]. Third, the ratio of CE volume to necrosis may be a surrogate for stressful metabolic conditions, including hypoxia and starvation. Finally, the CE parameters did not significantly differ between the proneural, neural, classical, and mesenchymal subtypes of glioblastoma.

The strengths of our study include application of an established, automated imaging segmentation algorithm [19] for analysis of clinical MRI, thereby minimizing the influence of subjective radiographic interpretation on study outcome. Importantly, this algorithm was previously demonstrated to yield results that were highly reproducible when compared to independent expert segmentations [21]. The larger sample size in our study relative to previous studies of CE in glioblastoma patients also affords statistical power for discovery. Nevertheless, there are limitations to our study that warrant comments. Our CE segmentation algorithm attempted to normalize the degree of contrast enhancement using the median intensity of the non-tumor blood vessels. However, scan time relative to contrast injection can differ between the institutions and may contribute CE variations unaccounted for by our method.

Additionally, differences in imaging acquisition from the multiple institutions participating in the TCIA/TCGA may yield unappreciated biases. Additionally, automated normalization procedures introduce potential systemic bias [43] that may confound the study result. Despite these limitations, the consistency between our study results and those previously published using distinct methods and diverse patient cohorts derived from studies using

evaluations by clinical radiologists [14,16,17,21] support the robustness of our findings

In summary, our results suggest that CE in glioblastoma MR imaging is an aggregate phenotype that reflects the extent of inflammation, tumor invasion, and stressful metabolic states. CE parameterization may facilitate rational utilization of therapeutics aimed to target these processes [44–46]. Due to the non-invasive nature of imaging biomarkers, information can be ascertained without subjecting patients to potential surgical morbidities. Furthermore, these biomarkers may augment the utility of tissue based genetic analysis or minimize delay in treatment decision. To these ends, future prospective validation of CE as an imaging biomarker will be needed. These studies will require an appropriate sample size as well as control for clinical variables such as corticosteroid use that may affect contrast enhancement.

5. Conclusions

Quantitative analysis of CE in glioblastoma tumors suggests that distinct aspects of CE reflect different physiologic states suggesting potential as an imaging biomarker. Further development of such biomarkers may provide means to non-invasively monitor the *in vivo* physiology of glioblastomas.

6. Sources of support

None.

7. Conflicts of interest

None.

References

[1] Ostrom QT, Gittleman H, Fulop J, Liu M, Blanda R, Kromer C, et al. CBTRUS statistical report: primary brain and central nervous system tumors diagnosed in the United States in 2008-2012. Neuro Oncol 2015;17(Suppl 4):iv1–iv62.

[2] Darefsky AS, King Jr JT, Dubrow R. Adult glioblastoma multiforme survival in the temozolomide era: a population-based analysis of surveillance, epidemiology, and end results registries. Cancer 2012;118:2163–72.

[3] Hegi ME, Diserens AC, Gorlia T, Hamou MF, de Tribolet N, Weller M, et al. MGMT gene silencing and benefit from temozolomide in glioblastoma. N Engl J Med 2005;352:997–1003.

[4] Esteller M, Garcia-Foncillas J, Andion E, Goodman SN, Hidalgo OF, Vanaclocha V, et al. Inactivation of the DNA-repair gene MGMT and the clinical response of gliomas to alkylating agents. N Engl J Med 2000;343:1350–4.

[5] Brennan CW, Verhaak RG, McKenna A, Campos B, Noushmehr H, Salama SR, et al. The somatic genomic landscape of glioblastoma. Cell 2013;155:462–77.

[6] Ng K, Kim R, Kesari S, Carter B, Chen CC. Genomic profiling of glioblastoma: convergence of fundamental biologic tenets and novel insights. J Neuro-oncol 2012;107:1–12.

[7] Burrell RA, McGranahan N, Bartek J, Swanton C. The causes and consequences of genetic heterogeneity in cancer evolution. Nature 2013;501:338–45.

[8] Rees JH, Smirniotopoulos JG, Jones RV, Wong K. Glioblastoma multiforme: radiologic-pathologic correlation. Radiographics 1996;16:1413–38. quiz 62-3.

[9] Gladwish A, Koh ES, Hoisak J, Lockwood G, Millar BA, Mason W, et al. Evaluation of early imaging response criteria in glioblastoma multiforme. Radiat Oncol 2011;6:121.

[10] Vredenburgh JJ, Desjardins A, Herndon 2nd JE, Marcello J, Reardon DA, Quinn JA, et al. Bevacizumab plus irinotecan in recurrent glioblastoma multiforme. J Clin Oncol 2007;25:4722–9.

[11] Claes A, Gambarota G, Hamans B, van Tellingen O, Wesseling P, Maass C, et al. Magnetic resonance imaging-based detection of glial brain tumors in mice after antiangiogenic treatment. Int J Cancer 2008;122:1981–6.

[12] Chamberlain MC. Bevacizumab for recurrent malignant gliomas: efficacy, toxicity, and patterns of recurrence. Neurology 2009;72:772–3. author reply 3-4.

[13] Ellingson BM, Cloughesy TF, Lai A, Nghiemphu PL, Mischel PS, Pope WB. Quantitative volumetric analysis of conventional MRI response in recurrent glioblastoma treated with bevacizumab. Neuro Oncol 2011;13:401–9.

[14] Jamshidi N, Diehn M, Bredel M, Kuo MD. Illuminating radiogenomic characteristics of glioblastoma multiforme through integration of MR imaging, messenger RNA expression, and DNA copy number variation. Radiology 2014;270:1–2.

[15] Carrillo JA, Lai A, Nghiemphu PL, Kim HJ, Phillips HS, Kharbanda S, et al. Relationship between tumor enhancement, edema, IDH1 mutational status, MGMT promoter methylation, and survival in glioblastoma. AJNR Am J Neuroradiol 2012;33:1349–55.

[16] Pope WB, Chen JH, Dong J, Carlson MRJ, Perlina A, Cloughesy TF, et al. Relationship between gene expression and enhancement in glioblastoma multiforme: exploratory DNA microarray analysis. Radiology 2008;249:268–77.

[17] Diehn M, Nardini C, Wang DS, McGovern S, Jayaraman M, Liang Y, et al. Identification of noninvasive imaging surrogates for brain tumor gene-expression modules. Procd Natal Acad Sci U S A 2008;105:5213–8.

[18] Wang K, Wang YY, Wang JF, Ma J, Jiang T, Dai JP. Radiologic features and expression of vascular endothelial growth factor stratify survival outcomes in patients with glioblastoma. AJNR Am J Neuroradiol 2016;37:629–35.

[19] Fischer I, Gagner JP, Law M, Newcomb EW, Zagzag D. Angiogenesis in gliomas: biology and molecular pathophysiology. Brain Pathol 2005;15:297–310.

[20] Rome C, Arsaut J, Taris C, Couillaud F, Loiseau H. MMP-7 (matrilysin) expression in human brain tumors. Mol Carcinog 2007;46:446–52.

[21] Steed TC, Treiber JM, Patel KS, Taich Z, White NS, Treiber ML, et al. Iterative probabilistic voxel labeling: automated segmentation for analysis of The Cancer Imaging Archive glioblastoma images. AJNR Am J Neuroradiol 2015;36:678–85.

[22] Jenkinson M, Bannister P, Brady M, Smith S. Improved optimization for the robust and accurate linear registration and motion correction of brain images. NeuroImage 2002;17:825–41.

[23] R Core Team. R: A language and environment for statistical computing. Vienna, Austria: R Foundation for Statistical Computing; 2017.

[24] Shannon CE, Weaver W. The mathematical theory of communication. Urbana: University of Illinois Press; 1949.

[25] Benjamini Y, Hochberg Y. Controlling the false discovery rate - a practical and powerful approach to multiple testing. J Roy Stat Soc B Met 1995;57:289–300.

[26] Huang DW, Sherman BT, Lempicki RA. Systematic and integrative analysis of large gene lists using DAVID bioinformatics resources. Nat Protoc 2009;4:44–57.

[27] Ashburner M, Ball CA, Blake JA, Botstein D, Butler H, Cherry JM, et al. Gene ontology: tool for the unification of biology. Gene Ontol Consortium Nat Genet 2000;25:25–9.

[28] Barbie DA, Tamayo P, Boehm JS, Kim SY, Moody SE, Dunn IF, et al. Systematic RNA interference reveals that oncogenic KRAS-driven cancers require TBK1. Nature 2009;462:108–12.

[29] Kidane D, Chae WJ, Czochor J, Eckert KA, Glazer PM, Bothwell ALM, et al. Interplay between DNA repair and inflammation, and the link to cancer. Crit Rev Biochem Mol Biol 2014;49:116–39.

[30] Golebiewska EM, Poole AW. Platelet secretion: from haemostasis to wound healing and beyond. Blood Rev 2015;29:153–62.

[31] Stokes KY, Granger DN. Platelets: a critical link between inflammation and microvascular dysfunction. J Physiol 2012;590:1023–34.

[32] van Zijl F, Krupitza G, Mikulits W. Initial steps of metastasis: cell invasion and endothelial transmigration. Mutat Res 2011;728:23–34.

[33] Hosseini Y, Agah M, Verbridge SS. Endothelial cell sensing, restructuring, and invasion in collagen hydrogel structures. Integr Biol (Camb) 2015;7:1432–41.

[34] Hatzikirou H, Basanta D, Simon M, Schaller K, Deutsch A. 'Go or grow': the key to the emergence of invasion in tumour progression? Math Med Biol 2012;29:49–65.

[35] Ng K, Nitta M, Hu L, Kesari S, Kung A, D'Andrea A, et al. A small interference RNA screen revealed proteasome inhibition as strategy for glioblastoma therapy. Clin Neurosurg 2009;56:107–18.

[36] Hanssum A, Zhong Z, Rousseau A, Krzyzosiak A, Sigurdardottir A, Bertolotti A. An inducible chaperone adapts proteasome assembly to stress. Mol Cell 2014;55:566–77.

[37] Adachi J, Kishida M, Watanabe S, Hashimoto Y, Fukamizu K, Tomonaga T. Proteome-wide discovery of unknown ATP-binding proteins and kinase inhibitor target proteins using an ATP probe. J Proteome Res 2014;13:5461–70.

[38] Jen J, Wang Y-C. Zinc finger proteins in cancer progression. J Biomed Sci 2016;23:53.

[39] Vartanian A, Singh SK, Agnihotri S, Jalali S, Burrell K, Aldape KD, et al. GBM's multifaceted landscape: highlighting regional and microenvironmental heterogeneity. Neuro-Oncology 2014;16:1167–75.

[40] Smirniotopoulos JG, Murphy FM, Rushing EJ, Rees JH, Schroeder JW. Patterns of contrast enhancement in the brain and meninges. Radiographics 2007;27:525–51.

[41] Forster C, Burek M, Romero IA, Weksler B, Couraud P-O, Drenckhahn D. Differential effects of hydrocortisone and TNFalpha on tight junction proteins in an in vitro model of the human blood-brain barrier. J Physiol 2008;586:1937–49.

[42] Seed M, Walsh DA. Angiogenesis in inflammation: mechanisms and clinical correlates: Birkhäuser Basel; 2008.

[43] Wang H, Das SR, Suh JW, Altinay M, Pluta J, Craige C, et al. A learning-based wrapper method to correct systematic errors in automatic image segmentation: consistently improved performance in hippocampus, cortex and brain segmentation. Neuroimage 2011;55:968–85.

[44] Mantovani A, Marchesi F, Malesci A, Laghi L, Allavena P. Tumour-associated macrophages as treatment targets in oncology. Nat Rev Clin Oncol 2017;14:399–416.

[45] Xie Q, Mittal S, Berens ME. Targeting adaptive glioblastoma: an overview of proliferation and invasion. Neuro-Oncology 2014;16:1575–84.

[46] Vander Heiden MG. Targeting cancer metabolism: a therapeutic window opens. Nat Rev Drug Discov 2011;10:671–84.